Journal of Materials Chemistry C

ROYAL SOCIETY OF CHEMISTRY

PAPER

View Article Online
View Journal | View Issue

Cite this: J. Mater. Chem. C, 2023, 11, 3095

$IrAu_{12}$ superatom modified by chiral diphosphines: doping-induced enhancement of chiroptical activity†

Haru Hirai, [a] Takuya Nakashima, *[bc] Shinjiro Takano, [a] Yukatsu Shichibu, [de] Katsuaki Konishi, *[de] Tsuyoshi Kawai [b] and Tatsuya Tsukuda *[a]

Received 14th December 2022,
Accepted 1st February 2023

DOI: 10.1039/d2tc05321g

rsc.li/materials-c

Gold superatoms modified by chiral ligands are a new class of chiroptical nanomaterials, but improvement of their chiroptical properties, such as circular dichroism (CD) and circularly polarized luminescence (CPL), remains a challenge. In this work, we studied the effects of single-atom doping on the chiroptical properties of a representative Au_{13} superatom using $[Au_{13}((R,R)\text{-DIPAMP})_5Cl_2]^{3+}$ and $[Au_{13}((S,S)\text{-DIPAMP})_5Cl_2]^{3+}$ (**Au_{13}-*R*/*S***; DIPAMP = 1,2-bis[(2-methoxyphenyl)phenylphosphino]ethane). We synthesized an enantiomeric pair of superatoms: $[IrAu_{12}((R,R)\text{-DIPAMP})_5Cl_2]^{+}$ and $[IrAu_{12}((S,S)\text{-DIPAMP})_5Cl_2]^{+}$ (**$IrAu_{12}$-*R*/*S***). Single-crystal X-ray diffraction analysis revealed that the icosahedral Ir@Au_{12} core of **$IrAu_{12}$-*R*/*S*** was more twisted along the Cl–Au–Ir–Au–Cl axis compared with the Au_{13} core of **Au_{13}-*R*/*S***, leading to a larger absorption anisotropy factor. **$IrAu_{12}$-*R*/*S*** exhibited a much higher photoluminescence quantum yield (~70%) compared with **Au_{13}-*R*/*S*** (15%) due to a larger energy gap between the highest occupied and the lowest unoccupied molecular orbitals. Although Ir doping did not appreciably enhance the photoluminescence anisotropy factors, the brightness of the CPL of **$IrAu_{12}$-*R*/*S*** was five times higher than that of **Au_{13}-*R*/*S***. This work provides a rational guide for improving the chiroptical activity of Au superatoms *via* the doping-mediated manipulation of the geometric and electronic structures.

Introduction

Ligand-protected gold (Au) and silver (Ag) superatoms with chiral structures have attracted growing interest as chiroptical nanomaterials because their atomically-precise structures make them ideal models for elucidating chiral structure–property correlations.[1–4] Since the first preparation of the optically active Au superatom protected by L-glutathione,[5] various enantiomeric superatoms have been synthesized using chiral ligands such as thiolates,[6–9] diphosphines,[10–14] alkynyls,[15] and N-heterocyclic carbenes.[16] Chiral superatoms also are obtained *via* the asymmetric arrangement of achiral ligands.[17–21] Chiral counterions have often been used for the optical resolution and asymmetric synthesis of such chiral superatoms with achiral ligands.[22–24] These superatoms and assemblies of them exhibit unique chiroptical properties such as circular dichroism (CD) and circularly polarized luminescence (CPL). The CD activity is determined by the absorption anisotropy factor (g_{abs}), whereas the CPL is evaluated by the brightness (B_{CPL}) as given *via* the following equation:[25]

$$B_{CPL} = \varepsilon \times \Phi_{PL} \times \frac{g_{PL}}{2} \quad (1)$$

where ε, Φ_{PL}, and g_{PL} are the molar absorption coefficient at the excitation wavelength, the photoluminescence (PL) quantum yield, and the PL anisotropy factor, respectively. For these superatoms, the anisotropy factors (g_{abs} and g_{PL}) are typically of the order of 10^{-3}, and the Φ_{PL} is less than 10%. Previous studies on the crystallization, self-assemby,[11,15,19,21] and doping of superatoms[26] have suggested the following strategies for improving these key parameters: (1) the g_{abs} value can be enhanced *via* torsion of the superatom[14] and by placing π-electron ligands in the vicinity of the superatom;[10,27] (2) the Φ_{PL} value can be

[a] Department of Chemistry, Graduate School of Science, The University of Tokyo, 7-3-1 Hongo, Bunkyo-ku, Tokyo 113-0033, Japan. E-mail: tsukuda@chem.s.u-tokyo.ac.jp
[b] Division of Materials Science, Nara Institute of Science and Technology (NAIST), 8916-5 Takayama, Ikoma, Nara 630-0192, Japan
[c] Department of Chemistry, Graduate School of Science, Osaka Metropolitan University, 3-3-138 Sugimoto, Sumiyoshi-ku, Osaka 558-8585, Japan
[d] Graduate School of Environmental Science, Hokkaido University, North 10 West 5, Sapporo 060-0810, Japan
[e] Faculty of Environmental Earth Science, Hokkaido University, North 10 West 5, Sapporo 060-0810, Japan

† Electronic supplementary information (ESI) available. CCDC 2225808 and 2225809. For ESI and crystallographic data in CIF or other electronic format see DOI: https://doi.org/10.1039/d2tc05321g

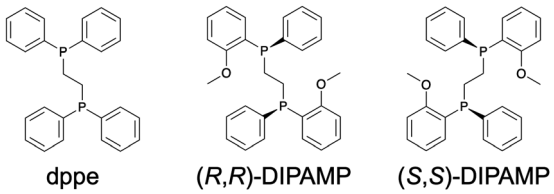

Chart 1 Diphosphine ligands used in this study.

enhanced through rigidification of the superatom and widening of the energy gap between the highest occupied molecular orbital (HOMO) and the lowest unoccupied molecular orbital (LUMO).[26]

To test the effectiveness of the above strategies, we herein studied the effects of single-atom doping on the chiroptical properties of a representative Au_{13} superatom protected by chiral diphosphine ligands (Chart 1; dppe = 1,2-bis(diphenylphosphino)ethane, DIPAMP = 1,2-bis[(2-methoxyphenyl)phenylphosphino]ethane), *i.e.*, $[Au_{13}((R,R)\text{-DIPAMP})_5Cl_2]^{3+}$ (**Au_{13}-*R***) and $[Au_{13}((S,S)\text{-DIPAMP})_5Cl_2]^{3+}$ (**Au_{13}-*S***).[13,14] Single-crystal X-ray diffraction (SCXRD) analysis showed that the icosahedral $Au@Au_{12}$ core consisted of a pair of Au_5 rings bridged by five DIPAMP ligands with a linear Cl–Au–Au–Au–Cl axis at their center (Fig. 1a). The degree of structural distortion of the $Au@Au_{12}$ core was evaluated *via* the dihedral angle of the two Au_5 rings (θ) (Fig. 1b). The average deviation of θ from that of a perfect icosahedron ($\Delta\theta = |36^\circ - \theta|$) was $1.19 \pm 0.61^\circ$ and $1.24 \pm 0.59^\circ$ for **Au_{13}-*R*/*S***, respectively.[14] The dopant chosen in this study was iridium (Ir), based on the following findings obtained using achiral diphosphine ligands (Chart 1), for $[Au_{13}(dppe)_5Cl_2]^{3+}$ (**Au_{13}-dppe**) and $[IrAu_{12}(dppe)_5Cl_2]^{+}$ (**$IrAu_{12}$-dppe**). First, the $\Delta\theta$ value increased from $1.03 \pm 0.95^\circ$ for **Au_{13}-dppe** to $1.69 \pm 0.50^\circ$ for **$IrAu_{12}$-dppe**, probably due to the smaller atomic radius of Ir (2.0 Å) compared with that of Au (2.1 Å).[28,29] Second, the Φ_{PL} value increased markedly from 11% for **Au_{13}-dppe** to ~70% for **$IrAu_{12}$-dppe**[26] due to the expansion of the HOMO–LUMO (HL) gap from 1.9 eV for **Au_{13}-dppe** to 2.3 eV for **$IrAu_{12}$-dppe**. These results suggest that the chiroptical properties of the Au_{13} superatom can be improved through manipulation of the geometric and electronic structures *via* single-atom doping with Ir. To test this hypothesis, we fleshly synthesized an enantiomeric pair of $Ir@Au_{12}$ superatoms: $[IrAu_{12}((R,R)\text{-DIPAMP})_5Cl_2]^{+}$ (**$IrAu_{12}$-*R***) and $[IrAu_{12}((S,S)\text{-DIPAMP})_5Cl_2]^{+}$ (**$IrAu_{12}$-*S***). The B_{CPL} values of the **$IrAu_{12}$-*R*/*S*** enantiomers were five times larger than those of the non-doped **Au_{13}-*R*/*S*** enantiomers, mainly due to the enhancement of Φ_{PL} (eqn (1)).

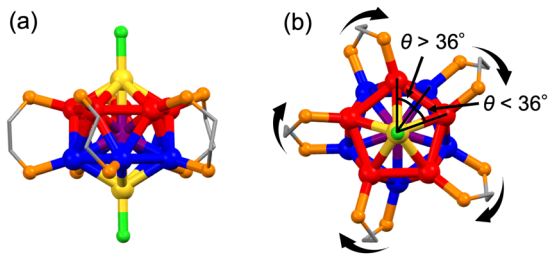

Fig. 1 (a) Side and (b) top view of the chiral structure of **MAu_{12}-dppe** (M = Ir, Au). Color code: yellow, Au the on Cl–Au–M–Au–Cl axis; red and blue, Au in the Au_5 rings; purple, M; orange, P; light green, Cl; gray, C.

Experimental section

Synthesis and characterization of $IrAu_{12}$-*R*/*S*·(PF_6)

The PF_6-salt of **$IrAu_{12}$-*R*/*S*** was synthesized according to the synthesis method for **$IrAu_{12}$-dppe**.[26] The **Au_{13}-*R*/*S*** enantiomers were also synthesized as a reference according to the method in ref. 14. Single crystals of **$IrAu_{12}$-*R*/*S***·(PF_6) suitable for SCXRD measurements were obtained *via* recrystallization from CH_2Cl_2/cyclopentyl methyl ether. Details of the synthesis and the characterization of **$IrAu_{12}$-*R*/*S*** are provided in the ESI.†

Optical and chiroptical measurements

The UV–Vis absorption spectra and CD spectra were recorded using a Jasco V-670 spectrometer and a JASCO J-725 spectropolarimeter, respectively. The g_{abs} values were calculated using the equation $g_{abs} = \theta$ [mdeg]/(32 980·Abs) using the CD (θ: ellipticity) and absorbance (Abs) data. PL spectra were recorded using a Jasco FP-8500 spectrofluorometer. The absolute value of Φ_{PL} was measured at ambient temperature using a Hamamatsu Photonics CC9920-02G assembly with an integration sphere. The PL lifetime measurements were carries out using a C4780 streak camera. The excitation source was generated using a Nd:YVO_4 laser (Verdi, Coherent) pumped Ti:sapphire laser system (Mira-900, Coherent) equipped with a cavity dumper (Pulse Switch, Coherent), which delivers 100 fs pulse trains at 800 nm. After doubling the frequency with a LiB_3O_5 crystal, the incident pulses were focused onto the samples (excitation wavelength = 400 nm). The PL decay curves were extracted from the 2D streak images in the range of 95 nm centered at the PL peak of each temperature. CPL spectra were recorded using a homemade CPL spectroscopy system equipped with a UV laser diode (375 nm) as the excitation source.[30] The g_{PL} values were calculated using the equation $g_{PL} = 2(I_L - I_R)/(I_L + I_R)$, where I_L and I_R are the PL intensity of the left and right circularly polarized light, respectively. An Ar-saturated solution was used for the PL and CPL measurements. The temperature for the PL and PL lifetime measurements was controlled in the range of 80–300 K using an Oxford Instruments OptistatDN liquid N_2 cryostat. For variable-temperature (VT) UV-Vis, CD, and CPL studies, the temperature of the samples was controlled in the range of 200–300 K using a Unisoku CoolSpeK cryogenic cell holder.

Results and discussion

Geometric structure

Isotopically resolved electrospray ionization (ESI) mass spectra of the **$IrAu_{12}$-*R*/*S*** samples confirmed the composition and charge state of $[IrAu_{12}(DIPAMP)_5Cl_2]^{+}$ (Fig. S1, ESI†). The mass spectra also exhibited small peaks at $m/z \approx 4963$, assigned to $[IrAu_{12}(DIPAMP)_5ClBr]^{+}$ (**$IrAu_{12}$-Br**) that originated from impurities in the chemicals used during the synthesis. Ratios of the

peak area of **IrAu$_{12}$-Br** to **IrAu$_{12}$-*R*/*S*** were 0.05 and 0.04, respectively, indicating that the purity of **IrAu$_{12}$-*R*/*S*** was ~95 mol%. The purities of the **IrAu$_{12}$-*R*/*S*** samples were further confirmed using ^{1}H NMR and elemental analysis. The ^{1}H NMR charts of the **IrAu$_{12}$-*R*/*S*** samples showed signals only for the DIPAMP ligands and the cyclopentyl methyl ether (CPME) used for crystallization (Fig. S2, ESI†). The ratio of the integrated signals indicated that the samples contained two equivalents of CPME to **IrAu$_{12}$-*R*/*S***. The elemental analysis demonstrated that **IrAu$_{12}$-*R*/*S*** contained 1.31 wt% of Cl, which was reproduced by considering that the samples consisted of 95 mol% of **IrAu$_{12}$-*R*/*S***·(PF_6)·$(CPME)_2$ and 5 mol% **IrAu$_{12}$-Br**·(PF_6)·$(CPME)_2$. Nevertheless, based on a previous report that the optical absorption profile and Φ_{PL} value of **Au$_{13}$-dppe** were hardly changed by replacing the Cl ligands with Br,[31] we concluded that the effect of the **IrAu$_{12}$-Br** impurity on the optical and chiroptical measurements was negligible.

The geometric structures of **IrAu$_{12}$-*R*/*S*** were solved *via* SCXRD analysis. The unit cell contained a single **IrAu$_{12}$-*R*/*S*** molecule and a PF_6 anion, supporting the monovalent charge state for **IrAu$_{12}$-*R*/*S*** as determined *via* ESI mass spectrometry. As shown in Fig. 2a, the **IrAu$_{12}$-*R*/*S*** enantiomers have an icosahedral $IrAu_{12}$ core ligated by five DIPAMP ligands and two Cl ligands. The position of the Ir atom could not been determined *via* SCXRD analysis due to the inability of distinguishing the electron density of Ir from Au. $^{31}P\{^1H\}$ NMR analysis was performed to reveal the location of Ir in the $IrAu_{12}$ core (Fig. S3, ESI†). The single peak in the $^{31}P\{^1H\}$ NMR charts of **IrAu$_{12}$-*R*/*S*** indicated that all ten phosphorus nuclei of the DIPAMP ligands were equivalent on the NMR time scale. Thus, the Ir atom was located at the center of the icosahedral core. The metal–metal bond lengths of **IrAu$_{12}$-*R*/*S*** and **Au$_{13}$-*R*/*S*** are summarized in Fig. S4 and Table S1 (ESI†). The average lengths of the Ir–Au bonds in **IrAu$_{12}$-*R*/*S*** were 2.726 ± 0.012 Å and 2.729 ± 0.017 Å, respectively, which were shorter than those of the corresponding radial Au–Au bonds in **Au$_{13}$-*R*/*S*** (2.761 ± 0.033 Å and 2.761 ± 0.034 Å, respectively).[14] The average lengths of the peripheral Au–Au bonds of **IrAu$_{12}$-*R*/*S*** (2.866 ± 0.026 Å and 2.870 ± 0.034 Å, respectively) were also shorter than those of **Au$_{13}$-*R*/*S*** (2.904 ± 0.030 Å and 2.903 ± 0.032 Å, respectively).[14] The contraction of the $Ir@Au_{12}$ core with respect to $Au@Au_{12}$ is due to the smaller van der Waals radius of Ir (2.0 Å) compared with that of Au (2.1 Å).[32] The torsion of the $Ir@Au_{12}$ core was quantified using the average value of $\Delta\theta$ (Fig. 2b). The values were 1.47 ± 0.30° and 1.89 ± 0.67° for **IrAu$_{12}$-*R*/*S***, respectively, which were larger than those of **Au$_{13}$-*R*/*S*** (1.19 ± 0.61° and 1.24 ± 0.59°, respectively).[14] These results indicated that the Au_5 rings of the $Ir@Au_{12}$ core were more twisted around the Cl–Au–Ir–Au–Cl axis compared with those of the Au_{13} core. In conclusion, the introduction of a smaller Ir atom to the Au_{13} core induced further distortion.

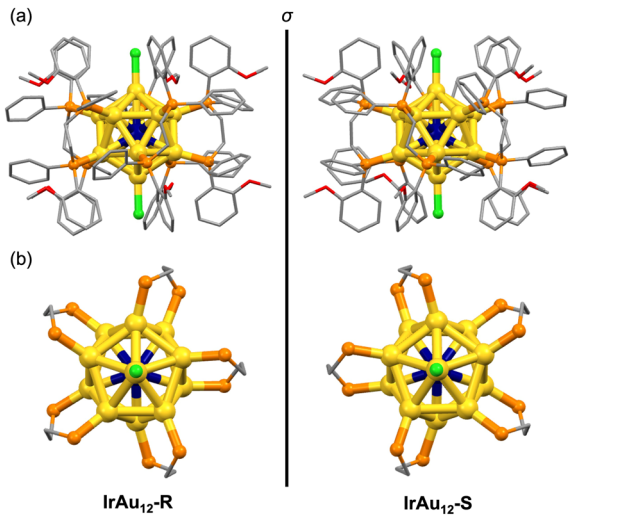

Fig. 2 (a) SCXRD structures of **IrAu$_{12}$-*R*** (left) and **IrAu$_{12}$-*S*** (right). Phenyl rings, ethylene bridges, and methoxy groups are depicted as sticks and hydrogen atoms are omitted for simplicity. (b) Top view of the core structures of **IrAu$_{12}$-*R*** (left) and **IrAu$_{12}$-*S*** (right). Phenyl rings and methoxy groups are omitted for simplicity. Color code: yellow, Au; dark blue, Ir; orange, P; light green, Cl; red, O; gray, C.

UV–Vis absorption and CD properties

The UV–Vis absorption spectra of **IrAu$_{12}$-*R*/*S*** (Fig. 3a) exhibited a distinct peak at 418 nm with an ε value of 2.08×10^4 M^{-1} cm^{-1} and 2.01×10^4 M^{-1} cm^{-1}, respectively. These ε values were larger than those of **Au$_{13}$-*R*/*S*** at 495 nm (1.61×10^4 M^{-1} cm^{-1} and 1.76×10^4 M^{-1} cm^{-1}, respectively) (Fig. 3b).[14] The onsets of the spectra revealed that the HL gaps of **IrAu$_{12}$-*R*/*S*** were 2.3 eV, which are larger than those of **Au$_{13}$-*R*/*S*** (1.9 eV) (insets of Fig. 3).[14] These results indicated the expansion of the HL gap upon Ir doping, as observed in **IrAu$_{12}$-dppe** and **Au$_{13}$-dppe** (Table 1).[26] Fig. S5 (ESI†) shows the VT UV–Vis spectra of **IrAu$_{12}$-*R*/*S*** in 2-methyltetrahydrofuran (MeTHF) recorded at 300 and 200 K. The spectrum at 200 K exhibited a sharper profile than that of the spectrum at 300 K because the hot band transition was suppressed at the lower temperature.[33–35] As a result, the two peaks at 420 and 470 nm became more pronounced and a new shoulder structure appeared at ~520 nm (the insets of Fig. S5, ESI†).

The VT CD spectra of **IrAu$_{12}$-*R*/*S*** are shown in Fig. 4a. The spectral profiles of the enantiomeric pair show a mirror image relationship, indicating the enantiopurity of the samples. The peak positions in the CD spectra at ~310, 340, 370, 400, 470,

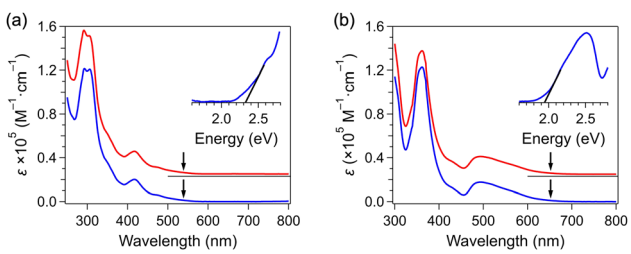

Fig. 3 UV–Vis absorption spectra of (a) **IrAu$_{12}$-*R*** (red) and **IrAu$_{12}$-*S*** (blue) in MeTHF and (b) **Au$_{13}$-*R*** (red) and **Au$_{13}$-*S*** (blue) in acetonitrile at ambient temperature. Arrows indicate the HL gaps estimated from the spectral onsets. Insets show the expanded spectra in the energy scale.

Table 1 Optical and chiroptical properties of **$IrAu_{12}$-*S*** and **Au_{13}-*S***

Superatom	HL gap (eV)	ε ($\times 10^4$ M^{-1} cm^{-1})	$\lvert g_{abs}\rvert$ ($\times 10^{-3}$)	λ_{PL} (nm)	Φ_{PL} (%)	τ_{PL} (μs)	λ_{CPL} (nm)	$\lvert g_{PL}\rvert$ ($\times 10^{-3}$)	Ref.
$IrAu_{12}$-*S*	2.3	2.01 (418 nm)	~4 (475 nm, 300 K) ~5 (475 nm, 200 K)	~609 (400 nm)	65.9	5.87	~600	~2 (600 nm, 300 K) ~4 (600 nm, 200 K)	
Au_{13}-*S*	1.9	1.76 (495 nm)	~2 (400 nm, 300 K) ~3 (400 nm, 200 K)	~792	15	3.19	~760	~2 (760 nm, 300 K) ~(4–5) (760 nm, 200 K)	13

The numbers in parentheses represent the excitation wavelength.

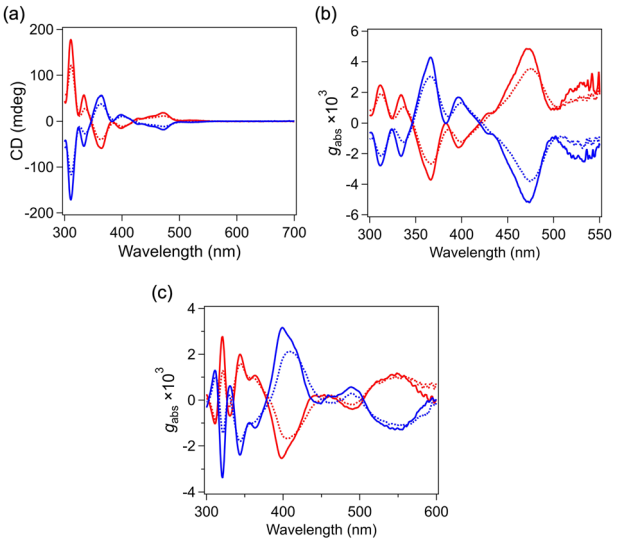

Fig. 4 (a) CD spectra and (b) g_{abs} spectra of **$IrAu_{12}$-*R*** (red) and **$IrAu_{12}$-*S*** (blue) in MeTHF. (c) g_{abs} spectra of **Au_{13}-*R*** (red) and **Au_{13}-*S*** (blue) in a MeOH–EtOH mixture (1 : 1 v/v). Solid and dotted lines denote the spectra recorded at 200 and 300 K, respectively.

and 530 nm corresponded to the absorption peaks and shoulder at ~305, 350, 420, 470 and 520 nm, respectively. The CD response for **$IrAu_{12}$-*R*/*S*** in the visible region is associated with the optical transition within the chiral Ir@Au_{12} core since the frontier orbitals are assigned to superatomic orbitals according to density functional theory calculations.[26] The $\lvert g_{abs}\rvert$ spectra of **$IrAu_{12}$-*R*/*S*** and **Au_{13}-*R*/*S*** are presented in Fig. 4b and c, respectively. The $\lvert g_{abs}\rvert$ values of **$IrAu_{12}$-*R*/*S*** are ~3 × 10^{-3} at 365 nm and ~4 × 10^{-3} at 475 nm, respectively, at 300 K (Table 1). By contrast, the maximum $\lvert g_{abs}\rvert$ value for **Au_{13}-*R*/*S*** was ~2 × 10^{-3} at 400 nm at 300 K (Table 1), which is consistent with the reported value.[13] According to the theoretical study in ref. 13, the higher $\lvert g_{abs}\rvert$ value for **$IrAu_{12}$-*R*/*S*** compared with that for **Au_{13}-*R*/*S*** is ascribed to the larger torsion of the Ir@Au_{12} core. The CD intensity of **$IrAu_{12}$-*R*/*S*** was enhanced by lowering the temperature from 300 to 200 K (Fig. 4a). The $\lvert g_{abs}\rvert$ value increased at 200 K to ~4 × 10^{-3} at 365 nm and ~5 × 10^{-3} at 474 nm, respectively (Fig. 4b, Table 1). The enhancement at the lower temperature is probably associated with the suppression of the thermal fluctuation of the Ir@Au_{12} core structure. A similar temperature dependence was observed for the $\lvert g_{abs}\rvert$ values of **Au_{13}-*R*/*S*** (Fig. 4c). The $\lvert g_{abs}\rvert$ value at 400 nm was enhanced to ~3 × 10^{-3} by lowering the temperature to 200 K (Table 1).

PL and CPL properties

The PL spectra of **$IrAu_{12}$-*S*** were recorded in de-aerated MeTHF (Fig. 5a). The PL peak of **$IrAu_{12}$-*S*** appeared at 609 nm at ambient temperature, which was shorter than that of **Au_{13}-*R*/*S*** (792 nm).[14] This blueshift reflects the expansion of the HL gap by the doping with Ir. The Φ_{PL} values of **$IrAu_{12}$-*R*/*S*** in MeTHF at 300 K were 69.9% and 65.9%, respectively(Fig. S6, ESI† and Table 1), and were much higher than the reported value of **Au_{13}-*R*/*S*** (15%).[14] The time-resolved PL decay of **$IrAu_{12}$-*S*** and **Au_{13}-*S*** was also measured (Fig. 5b and Fig. S7, ESI†). The PL lifetime (τ_{PL}), obtained through fitting with a single exponential function, of **$IrAu_{12}$-*S*** (5.87 μs) was longer than that of **Au_{13}-*S*** (3.19 μs) (Table 1). The increase in Φ_{PL} and τ_{PL} associated with the expansion of the HL gap was consistent with the case of **$IrAu_{12}$-dppe** and **Au_{13}-dppe**. According to the energy gap law, an increase in the PL energy suppresses the nonradiative relaxation process.[36]

The VT CPL spectra of **$IrAu_{12}$-*R*/*S*** and **Au_{13}-*R*/*S*** were recorded in de-aerated MeTHF and a MeOH–EtOH mixture (1 : 1 v/v), respectively (Fig. 6). The spectral profiles of the enantiomeric pairs of both samples are mirror images. The CPL bands peaked at ~600 and ~760 nm for **$IrAu_{12}$-*R*/*S*** and **Au_{13}-*R*/*S***, respectively, which are comparable to the positions of the corresponding PL bands at 300 K. The $\lvert g_{PL}\rvert$ values for **$IrAu_{12}$-*R*/*S*** at 300 K were ~3 × 10^{-3} and ~2 × 10^{-3}, respectively (Table 1), whereas those for **Au_{13}-*R*/*S*** were ~2 × 10^{-3}, which are comparable to the reported values (2.5 × 10^{-3} and −2.3 × 10^{-3} for **Au_{13}-*R*/*S***, respectively).[14] Note that the different $\lvert g_{PL}\rvert$ values between **$IrAu_{12}$-*R*/*S*** are due to the limited sensitivity of the CPL measurement setup. The similarity of the $\lvert g_{PL}\rvert$ values between **$IrAu_{12}$-*R*/*S*** and **Au_{13}-*R*/*S*** is probably associated with the similar structures in the photoexcited state responsible for PL. The $\lvert g_{PL}\rvert$ values of **$IrAu_{12}$-*R*/*S*** and **Au_{13}-*R*/*S*** increased to ~4 × 10^{-3} and ~(4–5) × 10^{-3}, respectively, upon lowering

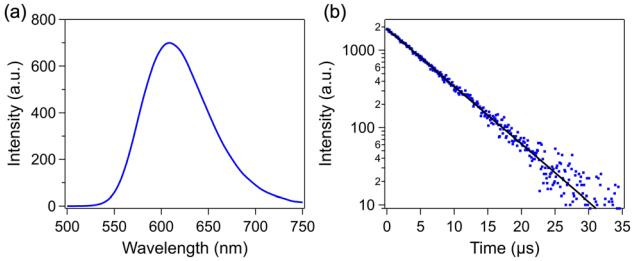

Fig. 5 (a) PL spectrum of **$IrAu_{12}$-*S*** in MeTHF recorded at the excitation wavelength of 400 nm. (b) Time-resolved PL decay of **$IrAu_{12}$-*S*** probed at 400 nm in MeTHF. The black line represents the fitting result.

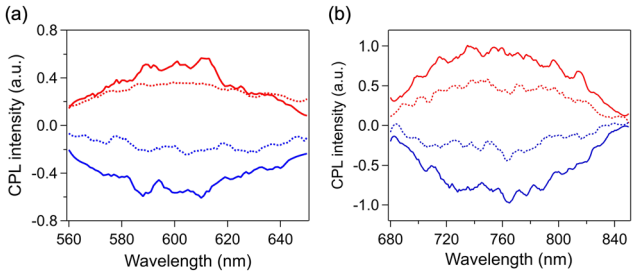

Fig. 6 CPL spectra of (a) **IrAu$_{12}$-*R*** (red) and **IrAu$_{12}$-*S*** (blue) in MeTHF and (b) **Au$_{13}$-*R*** (red) and **Au$_{13}$-*S*** (blue) in a MeOH–EtOH mixture (1 : 1 v/v) recorded at the excitation wavelength of 375 nm. Solid and dotted lines denote the spectra recorded at 200 and 300 K, respectively.

the temperature to 200 K (Fig. 6 and Table 1). The $|g_{PL}|$ values of **IrAu$_{12}$-*R*/*S*** were of the same order ($\sim 10^{-3}$) as those reported for other superatoms, whereas the Φ_{PL} values of **IrAu$_{12}$-*R*/*S*** were much higher than those of other chiral superatoms in either the solid or self-assembled state.[11,15,19,21] Therefore, **IrAu$_{12}$-*R*/*S*** are superior in terms of the CPL brightness (B_{CPL}) defined using eqn (1).[25] The B_{CPL} value of **IrAu$_{12}$-*S*** was 26 M^{-1} cm^{-1} (λ = 418 nm) at 300 K. This value is approximately five times higher than that of **Au$_{13}$-*S*** (B_{CPL} = 5.3 M^{-1} cm^{-1}, λ = 495 nm) at 300 K, indicating that doping with Ir brightened the CPL, mainly by increasing the molar absorption coefficient at 495 nm and the HL gap of **Au$_{13}$-*R*/*S***.

Conclusions

We successfully synthesized the enantiomeric pair of Ir@Au$_{12}$ superatoms protected by DIPAMP chiral diphosphine ligands and studied the single-atom doping effect on the chiroptical properties of the Au@Au$_{12}$ superatoms. The icosahedral Ir@Au$_{12}$ superatom was distorted more than the corresponding Au@Au$_{12}$, resulting in larger $|g_{abs}|$ values for the former. Doping with the Ir atom expanded the HOMO–LUMO gap of the Au$_{13}$ superatom, leading to the marked increase in Φ_{PL} from 15% to ~70%. By contrast, the $|g_{PL}|$ values of the IrAu$_{12}$ and Au$_{13}$ superatoms were comparable. As a whole, the CPL brightness of the Au$_{13}$ superatom was enhanced by nearly five times upon introducing Ir at the center. This work provides a new strategy to enhance the CPL brightness of Au superatoms *via* the doping-mediated control of geometric and electronic structures.

Author contributions

Haru Hirai: data curation, investigation, writing – original draft. Takuya Nakashima: formal analysis, investigation. Shinjiro Takano: conceptualization, investigation. Yukatsu Shichibu: data curation, methodology. Katsuaki Konishi: data curation, methodology. Tsuyoshi Kawai: resource. Tatsuya Tsukuda: funding acquisition, project administration, supervision, writing – review and editing. Each author contributed substantially to the manuscript.

Conflicts of interest

There are no conflicts to declare.

Acknowledgements

This research was financially supported by JST, CREST (Grant No. JPMJCR20B2) and JSPS KAKENHI (Grant No. JP20H00370 and JP20J21726). This work was partly supported by the Photo-excitonix Project at Hokkaido University.

Notes and references

1 S. Knoppe and T. Bürgi, *Acc. Chem. Res.*, 2014, **47**, 1318–1326.
2 Y. Li, T. Higaki, X. Du and R. Jin, *Adv. Mater.*, 2020, **32**, 1905488.
3 Y. Zhu, J. Guo, X. Qiu, S. Zhao and Z. Tang, *Acc. Mater. Res.*, 2021, **2**, 21–35.
4 Y. Shichibu and K. Konishi, *ChemNanoMat*, 2022, **8**, e202200194.
5 T. G. Schaaff, G. Knight, M. N. Shafigullin, R. F. Borkman and R. L. Whetten, *J. Phys. Chem. B*, 1998, **102**, 10643–10646.
6 S. Si, C. Gautier, J. Boudon, R. Taras, S. Gladiali and T. Bürgi, *J. Phys. Chem. C*, 2009, **113**, 12966–12969.
7 S. Knoppe, A. C. Dharmaratne, E. Schreiner, A. Dass and T. Bürgi, *J. Am. Chem. Soc.*, 2010, **132**, 16783–16789.
8 K. R. Krishnadas, L. Sementa, M. Medves, A. Fortunelli, M. Stener, A. Fürstenberg, G. Longhi and T. Bürgi, *ACS Nano*, 2020, **14**, 9687–9700.
9 T. Nakashima, R. Tanibe, H. Yoshida, M. Ehara, M. Kuzuhara and T. Kawai, *Angew. Chem., Int. Ed.*, 2022, **61**, e202208273.
10 S. Takano and T. Tsukuda, *J. Phys. Chem. Lett.*, 2016, **7**, 4509–4513.
11 L. Shi, L. Zhu, J. Guo, L. Zhang, Y. Shi, Y. Zhang, K. Hou, Y. Zheng, Y. Zhu, J. Lv, S. Liu and Z. Tang, *Angew. Chem., Int. Ed.*, 2017, **56**, 15397–15401.
12 J.-Q. Wang, Z.-J. Guan, W.-D. Liu, Y. Yang and Q.-M. Wang, *J. Am. Chem. Soc.*, 2019, **141**, 2384–2390.
13 Y. Yang, Q. Zhang, Z.-J. Guan, Z.-A. Nan, J.-Q. Wang, T. Jia and W.-W. Zhan, *Inorg. Chem.*, 2019, **58**, 3670–3675.
14 Y. Shichibu, Y. Ogawa, M. Sugiuchi and K. Konishi, *Nanoscale Adv.*, 2021, **3**, 1005–1011.
15 M.-M. Zhang, X.-Y. Dong, Z.-Y. Wang, X.-M. Luo, J.-H. Huang, S.-Q. Zang and T. C. W. Mak, *J. Am. Chem. Soc.*, 2021, **143**, 6048–6053.
16 R. W. Y. Man, H. Yi, S. Malola, S. Takano, T. Tsukuda, H. Häkkinen, M. Nambo and C. M. Crudden, *J. Am. Chem. Soc.*, 2022, **144**, 2056–2061.
17 I. Dolamic, S. Knoppe, A. Dass and T. Bürgi, *Nat. Commun.*, 2012, **3**, 798.
18 H. Yoshida, M. Ehara, U. D. Priyakumar, T. Kawai and T. Nakashima, *Chem. Sci.*, 2020, **11**, 2394–2400.
19 S. Chen, W. Du, C. Qin, D. Liu, L. Tang, Y. Liu, S. Wang and M. Zhu, *Angew. Chem., Int. Ed.*, 2020, **59**, 7542–7547.
20 H. Yi, K. M. Osten, T. I. Levchenko, A. J. Veinot, Y. Aramaki, T. Ooi, M. Nambo and C. M. Crudden, *Chem. Sci.*, 2021, **12**, 10436–10440.

21 X. Q. Liang, Y. Z. Li, Z. Wang, S. S. Zhang, Y. C. Liu, Z. Z. Cao, L. Feng, Z. Y. Gao, Q. W. Xue, C. H. Tung and D. Sun, *Nat. Commun.*, 2021, **12**, 4966.
22 S. Knoppe, O. A. Wong, S. Malola, H. Häkkinen, T. Bürgi, T. Verbiest and C. J. Ackerson, *J. Am. Chem. Soc.*, 2014, **136**, 4129–4132.
23 H. Yao and M. Iwatsu, *Langmuir*, 2016, **32**, 3284–3293.
24 J. Yan, H. Su, H. Yang, C. Hu, S. Malola, S. Lin, B. K. Teo, H. Häkkinen and N. Zheng, *J. Am. Chem. Soc.*, 2016, **138**, 12751–12754.
25 L. Arrico, L. di Bari and F. Zinna, *Chem. – Eur. J.*, 2021, **27**, 2920–2934.
26 H. Hirai, S. Takano, T. Nakashima, T. Iwasa, T. Taketsugu and T. Tsukuda, *Angew. Chem., Int. Ed.*, 2022, **61**, e202207290.
27 N. Shinjo, S. Takano and T. Tsukuda, *Bull. Korean Chem. Soc.*, 2021, **42**, 1265–1268.
28 Y. Shichibu and K. Konishi, *Small*, 2010, **6**, 1216–1220.
29 H. Hirai, S. Takano, T. Nakamura and T. Tsukuda, *Inorg. Chem.*, 2020, **59**, 17889–17895.
30 H. Tsumatori, T. Nakashima and T. Kawai, *Org. Lett.*, 2010, **12**, 2362–2365.
31 Z.-H. Gao, J. Dong, Q.-F. Zhang and L.-S. Wang, *Nanoscale Adv.*, 2020, **2**, 4902–4907.
32 S. S. Batsanov, *Inorg. Mater.*, 2001, **37**, 871–885.
33 M. S. Devadas, S. Bairu, H. Qian, E. Sinn, R. Jin and G. Ramakrishna, *J. Phys. Chem. Lett.*, 2011, **2**, 2752–2758.
34 H. C. Weissker, H. B. Escobar, V. D. Thanthirige, K. Kwak, D. Lee, G. Ramakrishna, R. L. Whetten and X. López-Lozano, *Nat. Commun.*, 2014, **5**, 3785.
35 Y. Negishi, T. Nakazaki, S. Malola, S. Takano, Y. Niihori, W. Kurashige, S. Yamazoe, T. Tsukuda and H. Häkkinen, *J. Am. Chem. Soc.*, 2015, **137**, 1206–1212.
36 K. Kwak, V. D. Thanthirige, K. Pyo, D. Lee and G. Ramakrishna, *J. Phys. Chem. Lett.*, 2017, **8**, 4898–4905.

